Indian Crustal Front beneath Tibet Inferred from Seismic Anisotropy

Bingfeng Zhang[1,2], Xuewei Bao*[1], Yingkai Wu[1], Mengfan Jiang[1], and Kecheng Zhou[1]

Abstract

Postcollisional downgoing of the Indian plate has absorbed large amounts of the Cenozoic India–Asia convergence and is a key process governing the Tibetan Plateau's evolution and growth; however, to date, whether the Indian slab is currently subducting or underthrusting is still controversial. Here, we present new constraints on the nature of seismic anisotropy within the crust of the eastern Lhasa terrane and the adjacent areas by exploiting the splitting phenomenon of *P*-to-*S* converted phases from the Moho. A crustal seismic anisotropy dataset in the main collisional belt of Tibet is then assembled by incorporating the newly obtained and published measurements. Our results highlight the systematic changes in preferred orientation of deep-crust anisotropic minerals along the perpendicular direction of the Himalayan arc, with a sharp northward transition from convergence-parallel to orogen-parallel directions occurring at ~450 to 500 km north of the Main Frontal thrust. The latter observation provides an estimate of the northern frontier of the Indian lower crust from the perspective of seismic anisotropy and indicates overall and long-distance underthrusting of the Indian plate under Tibet.

Cite this article as Zhang, B., X. Bao, Y. Wu, M. Jiang, and K. Zhou (2024). Indian Crustal Front beneath Tibet Inferred from Seismic Anisotropy, *Seismol. Res. Lett.* **96**, 449–460, doi: 10.1785/0220240103.

Supplemental Material

Introduction

Continents collide after closure of oceans because of convergent forces of lateral ridge push, mantle drag, and high-angle slab pull (Li *et al.*, 2023). Although initially deemed unlikely, the capability for a buoyant continental plate to subduct has been extensively demonstrated by geophysical and geological evidences, as well as geodynamic simulations (Zheng, 2012; Li, 2013; Zhao *et al.*, 2015). Yet the real-world kinematic behaviors of the downgoing continental plate during continental collision vary from place to place and remain elusive. Taking the Tethyan domain that hosts several archetypical collisional systems, for example, the European slab subducts steeply under the western Alps (e.g., Zhao *et al.*, 2015), the Arabian plate underthrusts the Eurasia in a low angle beneath the Iranian plateau (e.g., Yang *et al.*, 2023), and in the Tibetan plateau further east, the dynamics of the collision zone seem to be more complex and less clear.

The Tibetan Plateau, the broadest and largest plateau on Earth with an average altitude of ~4500 m, was built on a tectonic collage created by a series of collisional events between Gondwana-derived terranes and the Asian continent since the Neoproterozoic to the early Paleozoic period (Zhang *et al.*, 2017; Wu *et al.*, 2020). From north to south, the Jinsha Suture (JS), the Bangong–Nujiang suture (BNS), and the Indus–Yarlung Tsangpo suture (IYS) document the geological history related to the opening and closure of Paleo-, Meso-, and Neo-Tethyan oceans, respectively (e.g., Yin, 2000). The hard collision between India and Asia was initiated at ~50 to 60 Ma after the closure of the Neo-Tethyan ocean (e.g., Tapponnier *et al.*, 2001; Hu *et al.*, 2016). Plate convergence is mostly accommodated by crustal shortening and thickening, as well as the recycling of the Indian–Tibetan lithosphere into the mantle (van Hinsbergen *et al.*, 2019; Wu *et al.*, 2022). These geodynamic processes have uplifted Tibet into a modern-like plateau (Ding *et al.*, 2022).

Competing hypotheses have been proposed regarding the kinematics of the consumed Indian slab. Li *et al.* (2008), based on the imaged northward-dipping high-velocity body down to the mantle transition zone depths, argued that the Indian slab began steep subduction prior to reaching the IYS (Fig. 1 inset, pink dashed line). Chen *et al.* (2017) showed a T-shaped high-wavespeed structure in the upper mantle of southern Tibet from adjoint tomography, interpreted as the superposition of the underthrusting Indian lithosphere extending to the JS and the delaminated Tibetan lithosphere beneath (Fig. 1 inset, red dashed line). Because slabs tend to advance farther in the

1. Key Laboratory of Geoscience Big Data and Deep Resource of Zhejiang Province, School of Earth Sciences, Zhejiang University, Hangzhou, China, https://orcid.org/0000-0003-1124-3481 (BZ); https://orcid.org/0000-0001-8836-405X (XB); https://orcid.org/0000-0001-9336-6631 (YW); https://orcid.org/0000-0002-1856-0992 (MJ); 2. Division of Mathematical Sciences, School of Physical and Mathematical Sciences, Nanyang Technological University, Singapore, Singapore

*Corresponding author: xwbao@zju.edu.cn

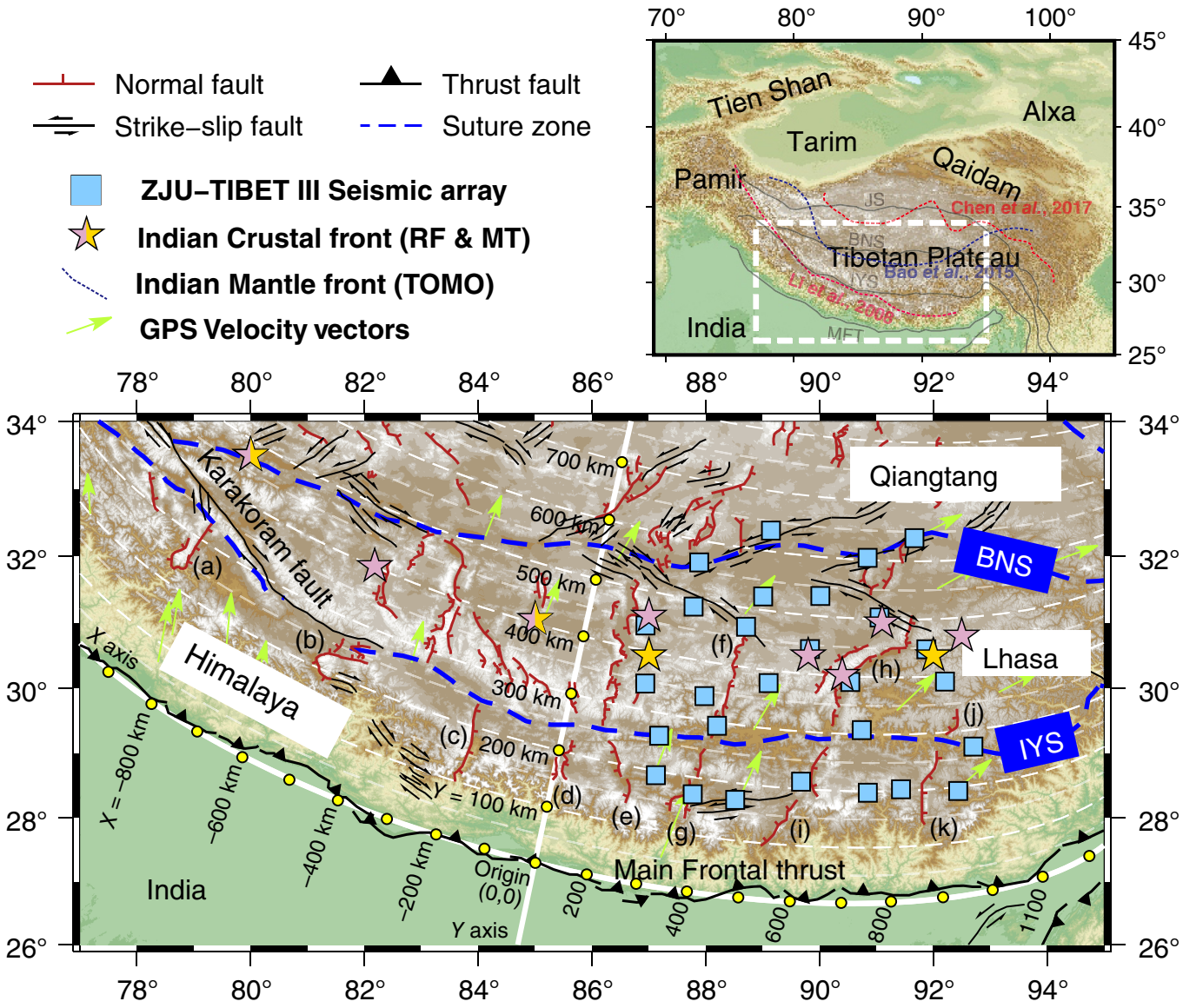

Figure 1. Shaded relief map of the main collisional belt of the Tibetan plateau. The locations of ZJU–Tibet III seismic stations used in this study are shown by blue-filled squares. Faults and suture zones are from Taylor and Yin (2009). White thick lines with annotations show *x* and *y* axes of the coordinate system used for the projection of anisotropy parameters along orogen-parallel and convergence-parallel directions in Figure 4. Green arrows denote Global Positioning System (GPS) velocities relative to the stable Eurasia plate (Gan *et al.*, 2007). Previously inferred Indian crustal front from receiver function (Kind *et al.*, 2002; Nábělek *et al.*, 2009; Zhang *et al.*, 2014; Shi *et al.*, 2016; Xu *et al.*, 2017) and magnetotelluric (Xie *et al.*, 2017) imaging are denoted by purple and yellow stars, respectively. The rifts mentioned in the Implications for crustal deformation in southern Tibet section and figures are labeled [(a) Leo Pargil, (b) Gurla Mandhata, (c) Thakkhola, (d) Gyirong, (e) Kung Co, (f) Xainza, (g) Dinggye, (h) Gulu, (i) Yadong, (j) Woka, and (k) Cona]. The sketch tectonic setting of the study area (white box) is indicated in the top right inset. In this inset, Indian mantle fronts delineated by seismic tomography studies (Li *et al.*, 2008; Bao *et al.*, 2015; Chen *et al.*, 2017) are denoted by dashed lines. BNS, Bangong–Nujiang suture; IYS, Indus–Yarlung suture; JS, Jinsha Suture; MFT, Main Frontal thrust; MT, magnetotelluric data; RF, receiver function; TOMO, tomography. The color version of this figure is available only in the electronic edition.

lateral direction when the dip angle is small (e.g., the low-angle underthrusting Nazca plate extends farther inboard under the South American plate than the steeply subducting counterpart; Hayes *et al.*, 2018), identifying the precise lateral extent of the disappearing India can help to illustrate the slab kinematics during India–Asia collision. However, no consensus has yet been reached regarding how far north the Indian plate has advanced beneath the plateau.

Aside from the aforementioned varying Indian mantle front (IMF), large discrepancies also exist for the inferred locations of Indian crustal front (ICF) at the top of the underthrusting Indian lithosphere. In *P*-wave receiver-function (P-RF) images

of southern Tibet, the widely observed two positive converted phases originated at the base of the crust (i.e., Moho doublet) are often regarded as the indictor of partially eclogitized Indian lower crust (e.g., Kind *et al.*, 2002; Nábělek *et al.*, 2009; Zhang *et al.*, 2014; Shi *et al.*, 2016; Xu *et al.*, 2017, 2022; Shi *et al.*, 2020). Its spatial extent suggests that the ICF has reached ∼33.5° N at ∼80° E, ∼31° N at ∼90° E and approximately follows the trend of the Himalayan arc (Fig. 1, purple stars). However, this long-distance underthrusting scenario has been questioned by several deep seismic-reflection profiles operated across the IYS that favor crustal-scale duplexing model with limited amounts of mafic Indian lower crustal materials extruding to the Lhasa terrane (e.g., Gao *et al.*, 2016; Guo *et al.*, 2017; Wang, Thybo, and Artemieva, 2021).

Seismic anisotropy at depths normally stems from lattice-preferred orientation of anisotropic minerals such as amphibole, mica, and olivine in response to tectonic strain (Silver, 1996; Savage, 1999). Therefore, constraining dominant seismic anisotropy signatures in the region can in turn provide valuable constraints on tectonic processes beneath. Shear-wave splitting, a commonly used and a robust technique to probe seismic azimuthal anisotropy, has been widely used to study the crustal deformation processes of the main collisional belt of Tibet. For local *S*-wave splitting reflecting upper-crustal anisotropy, delay times are generally small (<0.15 s), and fast polarization directions agree with stress directions or strike of local structures (Kanaujia *et al.*, 2019; Wu, Tian, Xu, Liang, Chen, Zhu, *et al.*, 2019; Guo and Gao, 2020; Roy *et al.*, 2021; Wang, Chang, and Ding, 2021; Hajra *et al.*, 2022; Liu *et al.*, 2023; Zhang *et al.*, 2023). *P*-to-*S* converted phases from the Moho (*Pms*) on P-RFs have also been exploited to constrain bulk anisotropy of the crust in Tibet (Zhang and Tian, 2011; Wu *et al.*, 2015; Paul *et al.*, 2017; Wu, Tian, Xu, Liang, Chen, Taylor, *et al.*, 2019; Huang *et al.*, 2021; Saikia *et al.*, 2022; Wadhawan *et al.*, 2022; Nie, Li, *et al.*, 2023). Zhang *et al.* (2023) quantified the *Pms* splitting characteristics in western–central Tibet using ZJU–Tibet I and II array data, which showed correlation between anisotropy and tectonic regimes and further illustrated the mechanisms underlying southern Tibetan rifting. Moreover, horizontal layering of crustal anisotropy has also been suggested by intracrustal converted phases on P-RFs (Ozacar and Zandt, 2004; Sherrington *et al.*, 2004; Schulte-Pelkum *et al.*, 2005; Liu *et al.*, 2015) and by ambient-noise and surface-wave tomography (Pandey *et al.*, 2015; Bao *et al.*, 2020).

This study builds on the work of Zhang *et al.* (2023), placing further constraints on the crustal azimuthal anisotropy properties in the eastern part of the main collisional belt using P-RF *Pms* moveout fitting technique and the newly retrieved ZJU–Tibet Phase III data. We also collect previous *Pms*-related anisotropy measurements within the main collisional belt to present a full picture of the lateral variations of crustal anisotropy there. Results of this analysis provide independent constraints on the Indian crustal front based on seismic anisotropy, a perspective different from previous studies, aiming to further illustrate the dynamical behaviors of the northward convergent Indian plate beneath Tibet. We also discuss the mechanisms responsible for southern Tibetan rifting and the possibility of large-scale crustal flow in southern Tibet.

Methods

As the third-phase deployment of ZJU–Tibet seismic array, 28 broadband seismographs were installed in the Lhasa and Tethyan Himalaya terranes between ∼87° and ∼93° E in June 2021 and were in operation until July 2022 (Fig. 1, blue squares). The teleseismic P-RFs analyzed in this study were retrieved from continuous recordings based on the event catalog information at the International Seismological Centre (minimum body-wave magnitude: 5.5; epicentral distance: 30°–90° to meet the requirement of steeply incident ray paths for P-RFs and to avoid secondary arrivals within the time window of interest). Well-recorded event waveforms (defined by signal-to-noise ratio > 15) are demeaned, detrended, and filtered to 0.02–1 Hz frequency band. We further use the water-level deconvolution technique (Ammon, 1991) to calculate radial P-RFs (water level: 0.1; gaussian coefficient: 1.5). After visual inspections of waveform quality, the P-RFs with clear *Pms* phases are selected and moveout corrected to 0.06 s/km (Chen and Niu, 2013) and then averaged in 10° back-azimuthal bins to mitigate the effect of uneven event distribution. Finally, 2374 radial P-RFs at 26 stations corresponding to 296 events are retained for later analyses (Fig. S1, available in the supplemental material to this article).

For a shear wave passing through the anisotropic medium, different degrees of splitting occur depending on the relationship between the back azimuth (θ) and the fast symmetry axis of the anisotropic medium, leading to systematic variations in phase arrival time with respect to back azimuth. In particular, for a single layer of anisotropy with a horizontal symmetry axis and a flat, horizontal layer interface, the *P*-to-*S* converted phase on the P-RFs exhibits a second-order harmonic variation ($\cos 2\theta$) as a function of back azimuth caused by a shear-wave splitting effect (Liu and Niu, 2012; Rümpker *et al.*, 2014), which can be used to quantify bulk azimuthal anisotropy properties between the surface and the *P*-to-*S* conversion depth. Here, we identify *Pms* phases on radial P-RFs based on the prior knowledge of crustal thicknesses in Tibet given by multidiscipline data such as gravity, tomography, and receiver-function *H-k* analyses (e.g., Bao *et al.*, 2015; Zhao *et al.*, 2020; Cheng *et al.*, 2022) and exploit the back-azimuthal variations of the *Pms* arrival times on bin-stacked radial P-RFs to constrain anisotropy parameters of the crust through least-squares fitting and grid search (Liu and Niu, 2012; Rümpker *et al.*, 2014; Zhang *et al.*, 2023). Seismic anisotropy parameters of interest include fast polarization direction (φ, short for polarization direction of fast-propagating shear wave and measured clockwise from the

north) and delay time (δt, short for delay time between observed arrivals of fast- and slow-propagating shear waves and reflecting magnitude of anisotropy). Ignoring third-order harmonic terms and beyond, the apparent *Pms* moveout can be expressed as (Li *et al.*, 2019; Zhang *et al.*, 2023)

$$t = t_0 + \frac{\alpha}{2}\cos(\theta - \beta) - \frac{\delta t}{2}\cos[2(\theta - \varphi)], \quad (1)$$

in which crustal seismic anisotropy parameters φ and δt are given by the second-order harmonic term in the equation, t_0 denotes *Pms* arrival time in isotropic model, α and β are amplitude and phase terms of the first-order harmonic variation ($\cos\theta$). It is noteworthy that first-order back-azimuthal harmonics are also considered in the earlier expression, which may result from structural complexities such as plunging symmetry axis of anisotropy or tilted Moho geometry, and frequently interfere with the quantification of second-order harmonics (Li *et al.*, 2019; Zhang *et al.*, 2023). For example, for rays coming from the up-dip directions of a tilted Moho, the arrival of *Pms* is delayed to different degrees with the latest arrival occurring at the dip direction because of elongated intracrustal prorogation path; the opposite is true for rays coming from the down-dip directions. In this study, the assumptions of a simple one-layered anisotropy and a horizontal symmetry axis for the analyses are justified because we measure the general anisotropic properties of the crust. The results indicate apparent anisotropy in the case of multiple anisotropic layers but can be mostly attributed to one layer when splitting induced by other layers are relatively weak. In addition, in the case of a plunging symmetry axis, φ varies little with plunging angle, and δt can be rescaled from that for the horizontal symmetry axis case (Nagaya *et al.*, 2008). To enhance the reliability of the resulting crustal anisotropy measurements, several requirements that must be met include sufficient back-azimuthal coverage, consistent results regardless of whether first-order harmonics is considered in the fitting scheme, small standard deviations calculated by bootstrapping, and small moveout residual (see Zhang *et al.*, 2023 for detailed descriptions of quality control criteria).

Results

After quality assessment, we obtain well-defined crustal anisotropy parameters at a total of 16 stations. An example for station TP-GAB is presented in Figure 2. All measurements are listed in Table S1 and presented in Figure S2. When we rotate horizontal-component P-RFs at a station into fast and slow components according to the measured φ, explicit polarity changes can be seen at φ-parallel or φ-normal back azimuths (Fig. S3, yellow stars), as in the synthetic case of a one-layered anisotropic crust model (Zhang *et al.*, 2023), indicating the reliability of these observations. Nevertheless, it is important to note that a single measurement is prone to the nonuniform back-azimuthal distribution of teleseismic events, the waveform complexities caused by data noise or Moho transition zone or sediment reverberations, and so forth. Therefore, we do not discuss the possible structural implications of station-specific measurements but rather focus only on the features that are persistent over a range of measurements.

To accomplish this, we further collected the published crustal anisotropy measurements from eight studies at a total of 127 seismic stations within the main collisional belt of Tibet (Zhang and Tian, 2011; Wu *et al.*, 2015; Paul *et al.*, 2017; Wu, Tian, Xu, Liang, Chen, Taylor, *et al.*, 2019; Huang *et al.*, 2021; Saikia *et al.*, 2022; Wadhawan *et al.*, 2022; Nie, Li, *et al.*, 2023), in addition to the measurements at 187 stations obtained in this and our previous studies (Zhang *et al.*, 2023). All studies exploit the splitting behavior of *Pms* phases on P-RFs when entering an anisotropic medium for quantification of seismic anisotropy, although different analysis schemes are used, such as *Pms* moveout fitting, *Pms* splitting, and *Pms* amplitude stacking. See Figure 3 for a map view of all φ estimates. The new observations provided in the present study fill the gap between ~87° and ~92° E in the Lhasa terrane, allowing for a clear and homogeneous distribution of information in the Tibetan area suitable for large-scale geodynamic implication. To better display the spatial variations in anisotropy parameters, we define a coordinate system (x–y) for projection of the results for which the x axis is a half ellipse ($\approx M^2/10.1^2 + N^2/3.4^2 = 1$) centered at (85.8° E, 30.6° N) and rotated 12.2° clockwise (Fig. 1, east–west white thick line), which closely fits the surface trace of main frontal thrust (MFT; curvature of the earth is neglected as in Jiao *et al.*, 2024). In addition, the y axis is the minor axis of this half ellipse (Fig. 1, north–south white thick line). The origin of the coordinate system (x = 0 km, y = 0 km) lies at the covertex of the half ellipse. The x and y axes approximate orogen-parallel and convergence-parallel directions, respectively. Figure 4 shows crustal anisotropy parameters arranged according to the x and y coordinates of seismic stations, respectively, to demonstrate orogen-parallel and convergence-parallel variations.

The first-order pattern of this expanded crustal anisotropy dataset across the main collisional belt of Tibet is largely consistent with our previous findings in its western–central part (Zhang *et al.*, 2023). Statistically speaking, the fast polarization directions (φ) show explicit north–south variations (Fig. 4a,b). In the sub-lesser-greater Himalaya terrane, the fast polarization directions are predominately orogen-parallel (east–west). Directions of φ rotate gradually in the Tethyan Himalaya terrane to convergence-parallel (north-northeast–south-southwest) and persist in this favorable orientation for most of the Lhasa terrane. At ~450 to 500 km north of the MFT, a sharp transition of fast polarization directions emerges, which changes from convergence-parallel in the south to orogen-parallel in the north. Spatial variations of φ in the east–west direction, on the other hand, are not very significant, except for the

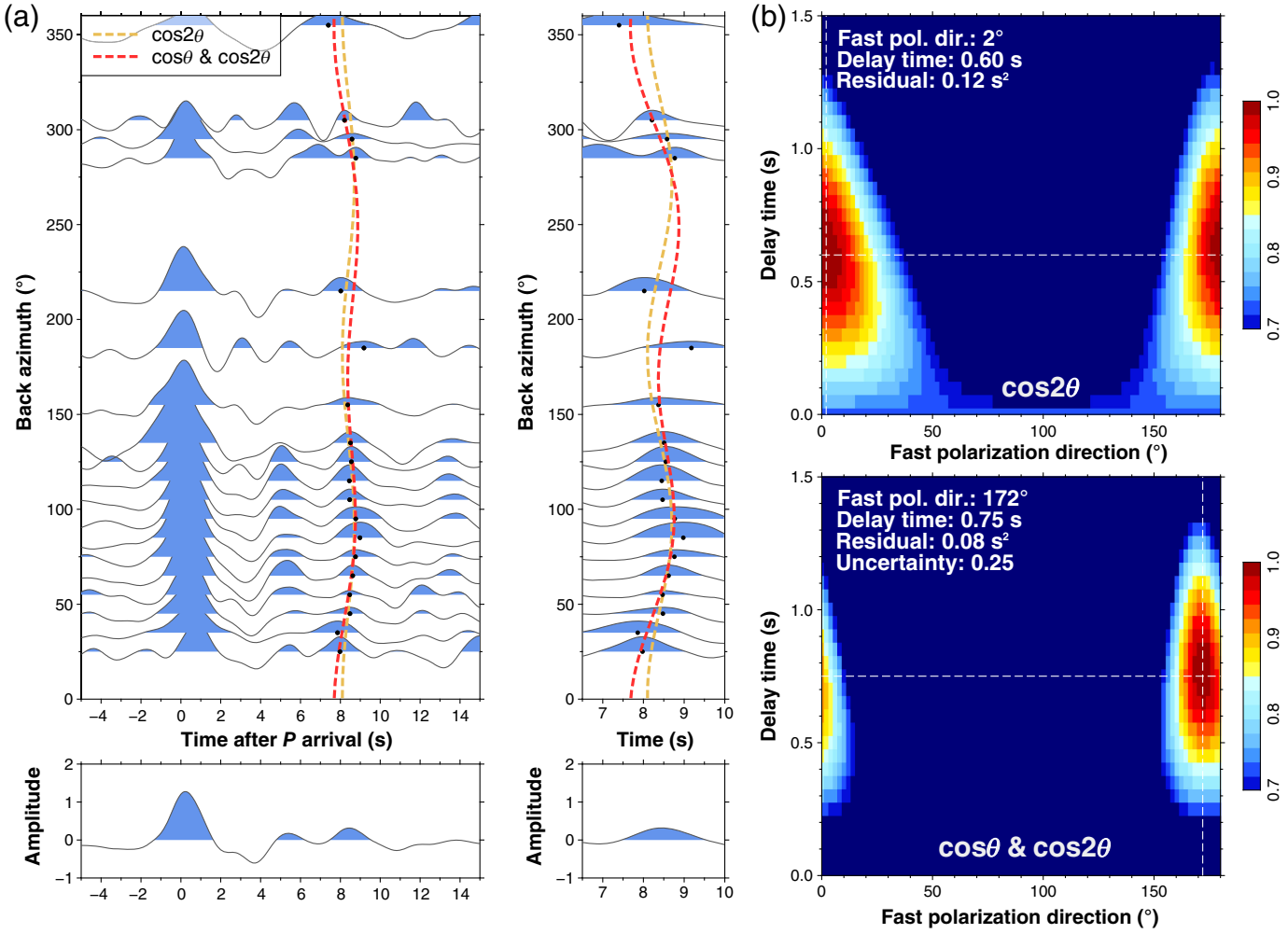

Figure 2. An example of *Pms* moveout fitting analysis for station TP-GAB. (a) Radial *P*-wave receiver function (P-RFs) plotted as a function of back azimuth and stacked P-RF. Arrival times of the *Pms* phases and the best-fit harmonic curves are indicated by black dots and dashed lines, respectively. (b) Energy maps showing the optimal pair of anisotropy parameters given by the second-order harmonic term of two *Pms* moveout fitting schemes with or without first-order harmonics considered. Pol. Dir., polarization direction. The color version of this figure is available only in the electronic edition.

clusters of anomalously oriented φ west of 79° E and east of 92° E in the Lhasa terrane (Fig. 4c). Different from φ, the delay times (δt) show less spatial variations (Fig. 4d, Fig. S4). The average δt for all measurements is 0.54 s, corresponding to V_S anisotropy of ~3.8% if we assume a 50-km-thick crust with an average V_S of 3.5 km/s, which implies an overall highly anisotropic crust underlies Tibet.

Discussion

Because of the steep incidence of the *Pms* ray paths, the resulting crustal anisotropy observations have little vertical resolution and are thus measures of apparent anisotropy of the entire crust. This issue can be remedied to some degree by the incorporation of *S*-wave splitting measurements of local shallow events that target only the upper crustal anisotropy (Fig. S5; Kanaujia *et al.*, 2019; Wu, Tian, Xu, Liang, Chen, Zhu, *et al.*, 2019; Guo and Gao, 2020; Roy *et al.*, 2021; Wang, Chang, and Ding, 2021; Hajra *et al.*, 2022; Liu *et al.*, 2023; Zhang *et al.*, 2023). In contrast to *Pms* observations, no preferred orientation can be explicitly distinguished either locally or regionally for local *S*-wave splitting dataset, suggesting that upper-crustal anisotropy contributes to *Pms* observations almost in a random sense. The upper crustal delay times beneath Tibet are generally <0.15 s, which are also significantly smaller than the δt estimates using *Pms* phases. Thus, the observed *Pms* anisotropy can be primarily attributed to the mid-lower crustal depths related to lattice-preferred orientation of anisotropic minerals. Particularly, anisotropy with fast-axis symmetry is produced by amphibole (Ko and Jung, 2015), the most abundant anisotropic mineral in the deep continental crust (Tatham *et al.*, 2008). Mica foliation with slow-axis symmetry plays a secondary role in midcrustal depths as mica content increases by granulite–amphibolite transition during retrograde metamorphism (Sherrington *et al.*, 2004; Mahan, 2006; Luo *et al.*, 2023). The

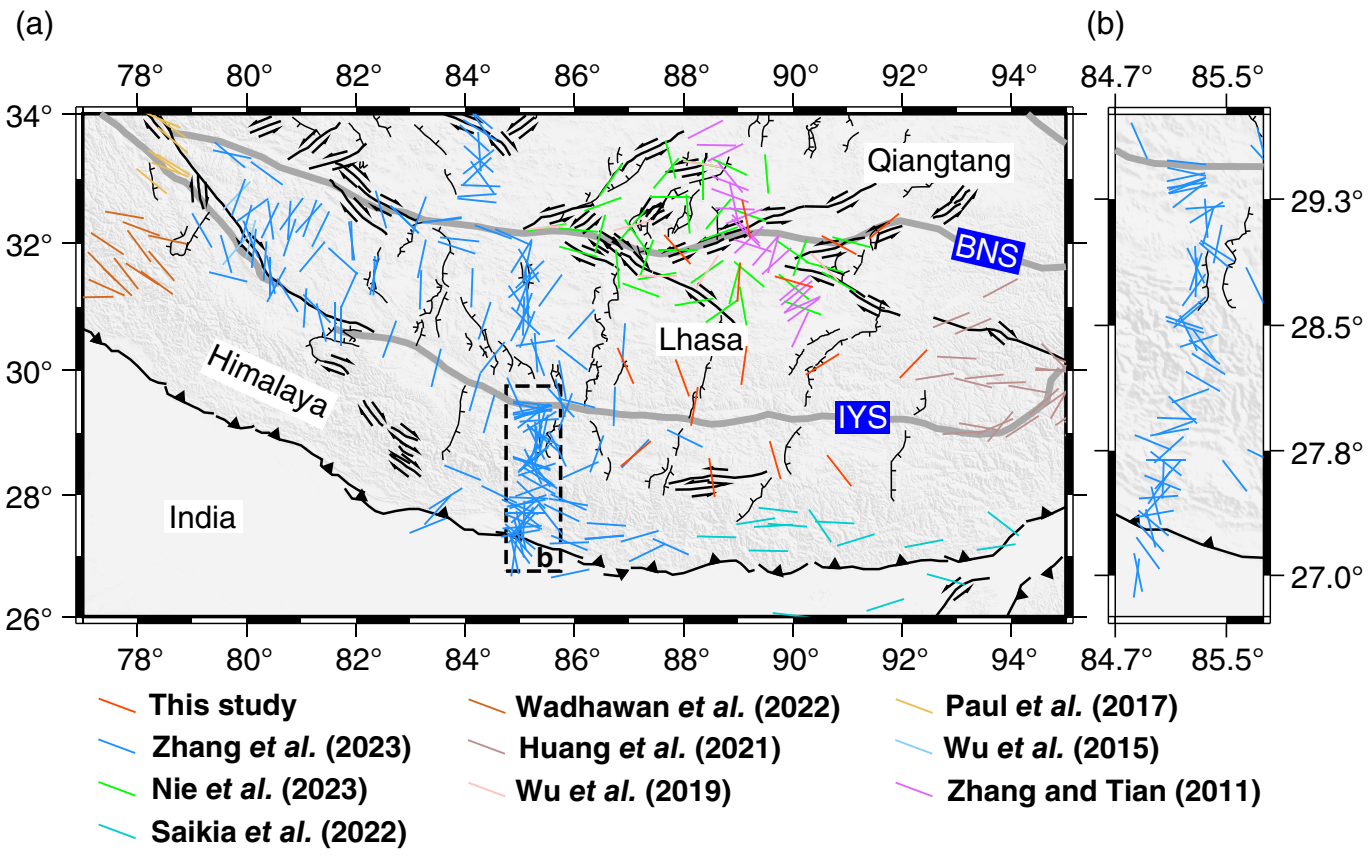

spatial patterns of *Pms* anisotropy serve as indicators of deformation patterns at depths and can provide critical constraints on a number of controversial issues regarding the geodynamic processes underlying the Tibetan Plateau. Here, we focus on two important yet debatable problems: the northern limit of the lost Indian crust and the crustal deformation of southern Tibet.

The inferred Indian crustal front from crustal anisotropy

The first issue is how far north the Indian crust has indented into Tibet. Previously inferred estimates differ and have not agreed on whether the Indian crustal materials have entered the Lhasa terrane or not (e.g., Nábělek *et al.*, 2009; Guo *et al.*, 2017). Generally speaking, alignments of dominant anisotropic minerals beneath the orogens are mostly subparallel to the orogen-parallel structural axis as a consequence of creeping deformation in response to orogen-perpendicular compressive stresses (Silver, 1996; Meissner *et al.*, 2002) or mantle flow regulated by subducting slab (Russo and Silver, 1994; Long and Silver, 2008). This is exactly the case in the northern part of the main collisional belt of Tibet where *Pms*, *Pn*, and *S(K)KS* anisotropy are all preferably oriented in the northeast-east–southwest-west to northwest-west–southeast-east directions (e.g., Lü *et al.*, 2011; Zhang *et al.*, 2023). Convergence-parallel anisotropy are not often observed but has been reported atop or below the underthrusting slab at some discrete locations beneath the orogens (e.g., central Tien Shan, Zhang *et al.*, 2022; Taiwan orogen, Huang *et al.*, 2015; and central Andes, Reiss *et al.*, 2018), related to simple shear between the convergent plates or between slab and ambient asthenospheric mantle (i.e., mantle wedge and uppermost sublithospheric mantle) in the context of the underthrusting process. Therefore, the spatial extent of convergence-parallel anisotropy against the background of orogen-parallel anisotropy can be used to indicate how far the underthrusting plate has advanced relative to the overriding plate.

Here, a marked transition of *Pms* fast polarization directions from convergence-parallel to orogen-parallel directions is seen at ~450 to 500 km north of the MFT (Fig. 4a). This boundary sits in the vicinity of BNS in western–central Tibet and extends to the central Lhasa terrane in regions farther east, which provides an independent estimate regarding the locations of Indian crustal front from the perspective of seismic anisotropy. This

Figure 3. Fast polarization directions of crustal seismic anisotropy in the main collisional belt of Tibet constrained by splitting phenomenon of *Pms* phases. (a) All measurements. Fast polarization directions are shown by the orientation of the bar line. Sources of each individual measurements are indicated by different colors. (b) A zoomed view of the measurements in Himalayan terrane along the Hi-CLIMB seismic line (Nábělek *et al.*, 2009). BNS, Bangong–Nujiang suture; IYS, Indus–Yarlung suture. The color version of this figure is available only in the electronic edition.

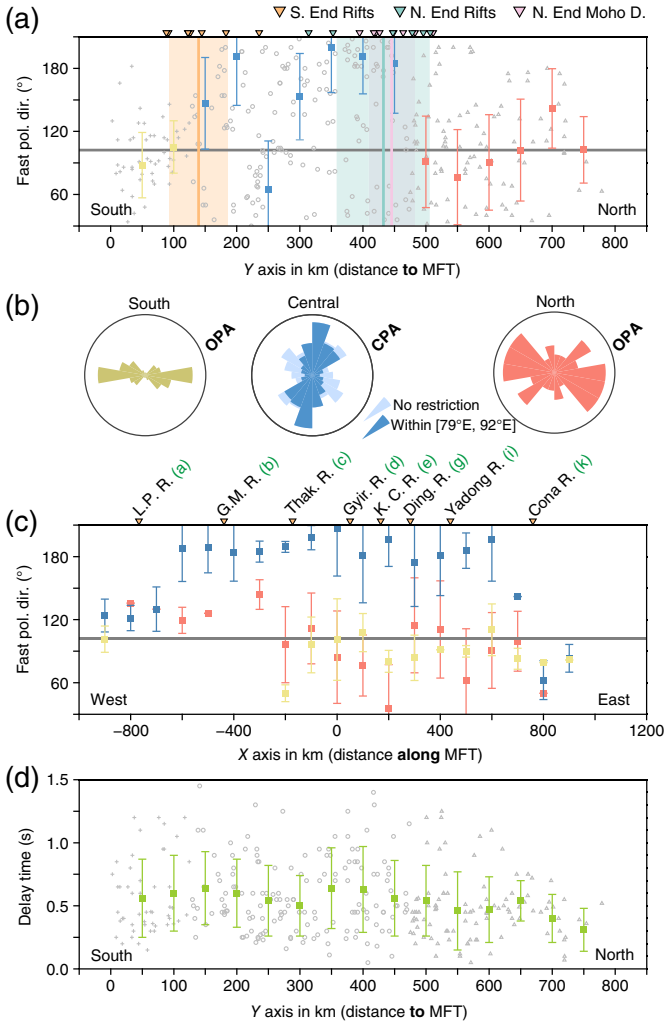

Figure 4. Fast polarization directions and delay times of crustal seismic anisotropy arranged in the convergence-parallel and orogen-parallel reference frame (*x*–y coordinate system). (a) Variations of fast polarization directions in the convergence-parallel direction. Colored squares with bars show average anisotropy parameters and their standard deviations within 70 km bins with 20 km overlapping. Anisotropy measurements are divided into three subregions based on the general trend of fast polarization directions (south: ~0 to 125 km, yellow; central: ~125 to 475 km, blue; north: ~475 km and above, red; distance is relative to main frontal thrust [MFT] based on *y* coordinates of seismic stations). Individual measurements within each subregions are shown by different kinds of symbols colored in gray (south: plus; central: circle; and north: triangle). The gray thick line marks the direction of major axis of the half ellipse used to construct the *x*–y coordinate system. Pink, orange, and blue-green inverted triangles show locations of northern termination of Moho doublet from P-RF imaging and southern and northern ends of southern Tibetan rifts, respectively. Their means and standard deviations are indicated by thick vertical lines and color-shaded backgrounds. (b) Rose diagrams showing statistics of fast polarization directions for different subregions. For the rose diagram in the middle, we make the plot with (light) blue color using all measurements within the central subregion and make the plot with (dark) blue color using only a subset of these measurements by excluding the two clusters of anomalous orogen-parallel observations west of 79° E and east of 92° E. (c) Variations of fast polarization directions in the orogen-parallel direction for each subregion. Colored squares with bars show average anisotropy parameters and their standard deviations within 140 km bins with 40 km overlapping. (d) Variations of delay times in the convergence-parallel direction. CPA, convergence-parallel anisotropy; Ding. R., Dinggye rift; G.M. R., Gurla Mandhata rift; Gyir. R., Gyirong rift; K. C. R., Kong Co rift; L.P. R., Leo Pargil rift; OPA, orogen-parallel anisotropy; Pol. Dir., polarization direction; Thak. R., Thakkhola rift. The color version of this figure is available only in the electronic edition.

estimate agrees well with the northern limits of Moho doublet signatures derived from receiver-function common conversion point imaging along several north–south-trending passive-seismic profiles across Tibet (Kind *et al.*, 2002; Nábělek *et al.*, 2009; Zhang *et al.*, 2014; Shi *et al.*, 2016; Xu *et al.*, 2017 (Fig. 1, purple stars). Previous studies regard the layer bounded by the Moho doublet as the partially eclogitized Indian lower crust (Hetényi *et al.*, 2007; Zhang *et al.*, 2014), which was transported northward along the Main Himalayan thrust (MHT, a northward gently dipping decollement in the Himalaya terrane that separates the Indian crust below from the Himalayan crust above). The relative (northward) movement of such layer with respect to the overriding in situ Tibetan crust can cause significant subhorizontal simple shear deformation adjacent to the shear plane, hence the seismic anisotropy observed in this region. This simple shear zone can also be traced back to the MHT, where Schulte-Pelkum *et al.* (2005) reported strong seismic anisotropy develops within a thin layer above the Himalayan decollement in response to shear processes. However, because the shallow (brittle) part of the MHT appears to be nearly fully locked (highly coupled; Ader *et al.*, 2012; Dal Zilio *et al.*, 2020), most shear stresses are elastically absorbed and released during large earthquakes. This leads to a limited amount of anelastic strain accumulated only near the MHT that is not able to manifest in the *Pms* observations.

Furthermore, our estimate is also consistent with the magnetotelluric imaging results that suggest the Indian crustal front has at least reached ~33.5° N along ~80° E, ~31° N along ~85° E, and ~ 30.5° N along ~87° E and ~92° E (Fig. 1, yellow stars), an inference based on the spatial coverage of the mid-lower crustal conductive layer atop the Indian plate induced by plate motion (Xie *et al.*, 2017). The reason for no visible upper-interface reflections in deep seismic reflection migration profiles may be related to the velocity transition zone structure at the top of the shear-deformed Indian lower crust and the different frequency contents of teleseismic (~1 Hz) and explosive-generated (~10 Hz) *P*-wave because the high-frequency waves are less sensitive to broad and gradual velocity interfaces (Liang *et al.*, 2023). In addition, because gravity data have shown that the partially eclogitized Indian lower crust beneath the Lhasa terrane is characterized by high density (Hetényi *et al.*, 2007; Xuan and Jin, 2022), it would tend to bend or delaminate rather than underthrust subhorizontally for over 400 km, as we observe here. This suggests that there exist some buoyant materials attached with the underthrusting Indian lower crust (e.g., the cratonic Indian mantle lithosphere) to prevent the overlying dense crust from sinking. This inference is in agreement with virtual deep seismic sounding and *S(K)KS* splitting results along Hi–CLIMB seismic line (Nábělek *et al.*, 2009) that show the ICF overlies the IMF (Chen *et al.*, 2010; Chen and Jiang, 2020) and with various tomographic evidences indicating that IMF extends farther north of the ICF (Bao *et al.*, 2015; Chen *et al.*, 2017; Li and Song, 2018). The underthrusting Indian lithosphere is thus vertically coupled in geometry and underthrusts northward as a whole with no detachment processes occurring between its crustal and mantle portions. Despite this general kinematic behavior, the Indian slab is still highly heterogenous as suggested by several local-scale low-velocity anomalies observed within the overall high-velocity slab (Bao *et al.*, 2015; Chen *et al.*, 2017; Li and Song, 2018). The locations of these anomalies coincide in general with the zones of minor subcrustal azimuthal anisotropy for which consistent *Pms*- and *S(K)KS*-derived φ are observed (Fig. S5c). Both observations suggest that there may be several local-scale asthenospheric upwelling channels through the slab potentially causing the higher $^3He/^4He$ as discovered in hot springs (Klemperer *et al.*, 2022). Furthermore, subhorizontal movement of the Indian slab also indicates that slab pull is not the primary driving force behind the India–Asia convergence after the break-off of Neo-Tethyan oceanic slab. Oceanic ridge push and mantle drag from the faster-moving asthenosphere, on the other hand, are more likely candidates (Becker and Faccenna, 2011; Li *et al.*, 2023).

Implications for crustal deformation in southern Tibet

Geological data indicate that rift extension is a widespread and prominent feature within the high plateau of Tibet, especially southern Tibet, where rifts are regularly spaced and >100 km long (Fig. 1). What drives east–west extension and active rifting in southern Tibet? In Zhang *et al.* (2023), on the basis of the spatial coincidence between convergence-parallel crustal anisotropy and western–central part of the southern Tibetan rift zone, we propose that strong north-directed shearing exerted by the underthrusting Indian plate is key to enabling present-day extension in southern Tibet. As shown in Figure 3, such patterns of convergence-parallel crustal anisotropy persist in regions farther east that cover the surface traces of Dinggye–Xainza (~88° E, labeled as "g" and "f" in Fig. 1) and Yadong–Gulu (~90° E, labeled as "" and "h") rifts, implying that such northward basal shear is probably a prevalent tectonic force taking effect under the entire southern Tibetan rift zone, contributing to the active upper crustal extension there. This is achieved by balancing the north–south compressional force from plate convergence and thereby reconfiguring the local stress field to the one that favors normal faulting (Copley *et al.*, 2011). Fast polarization directions rotate to east–west and northwest–southeast directions to the northeast of the Cona–Woka rift (labeled as "k" and "j" in Fig. 1) and to the northwest of the Leo Pargil rift (labeled as "a"), respectively, which can be attributed to processes such as vertically coherent pure shear thickening around the eastern Himalayan syntaxis (Huang *et al.*, 2021) and strike-slip motions along the Karakoram fault (Paul *et al.*, 2017). Alternatively, east–west-strike-slip motions could also cause the anomalous φ observations around the eastern Himalayan syntaxis when its total strength is high enough to mask the convergence-parallel fabrics directly related to basal shear. Such a hypothesized strike-slip component has been observed in this area (Li *et al.*, 2022) and has been successfully simulated using the tectonic geometry of eastern Himalayan syntaxis and tectonic forces, including basal shear, compression, and gravitational forces (Copley *et al.*, 2011). Therefore, it does not contradict the basal shear scenario.

Numerical modeling suggests that pronounced channel flow within the middle–lower crust would induce viscous buckling of the brittle upper crust, which is also capable of causing extension and rifting (Bischoff and Flesch, 2018). However, does large-scale eastward channel flow indeed exist in the main collisional belt of Tibet? The initiation of ductile flow of deep crustal materials requires a significant reduction in viscosity and lateral pressure gradients (Bird, 1991). The former requisite is often achieved by the partial melting of rocks in response to the elevated temperature, the addition of water, or both (McKenzie and Jackson, 2002). Because the Tibetan middle–lower crust is featured by high heat flow (Hacker *et al.*, 2000; Jiang *et al.*, 2019), slow seismic velocity (Yang *et al.*, 2012; Bao *et al.*, 2015; Huang *et al.*, 2020; Nie, Tian, *et al.*, 2023; Tan *et al.*, 2023), high conductivity (Wei *et al.*, 2001; Xie *et al.*, 2017; Jin *et al.*, 2022), strong attenuation (Fan and Lay, 2003; Zhao *et al.*, 2013), and high-V_P/V_S ratio (Gong *et al.*, 2023), the existence of partial melt is plausible in

some part of the Tibet. It is also noteworthy that channelized plastic flow in the deep crust can also result in azimuthal anisotropy with fast polarization direction subparallel to the shear (flow) direction under the conditions of high-differential stress and high temperature (Ko and Jung, 2015). However, the Lhasa and Tethyan Himalaya terranes are predominantly featured by north-northeast–south-southwest-trending non-flow-parallel *Pms* fast polarization directions (Fig. 3), suggesting that the presumed crustal flow there is insignificant (i.e., weak or thin) or even absent at the regional scale. Moreover, geophysical evidences of partial melting such as low velocity and low *Q* are lacking in the relatively thin southern Himalayan crust (Zhao *et al.*, 2013; Gilligan *et al.*, 2015) where east–west-oriented crustal anisotropy dominates (Fig. 3). Therefore, we conjecture that present-day large-scale eastward flow is unlikely to be well developed in southern Tibet, though there may be local-scale flow present at discrete locations given the isolated flow-parallel *Pms* observations, which is insignificant to the large-scale geodynamics in Tibet. These notions are also supported by limited connectivity of these potential partial melt zones as suggested by the aforementioned geophysical anomalies (e.g., Jin *et al.*, 2022; Gong *et al.*, 2023; Tan *et al.*, 2023) and insufficient amounts of viscosity drop for inducing channel flow given the estimated melt volume percentage of <7% there (Nie, Tian, *et al.*, 2023).

Conclusions

In this study, we established crustal anisotropy properties in the eastern part of the Lhasa terrane in Tibet by performing P-RF *Pms* moveout fitting analyses using ZJU–Tibet Phase III data. Combined with published measurements across the main collisional belt, we show that the orientation of seismic anisotropy in the mid-lower crust varies systematically in the direction perpendicular to Himalaya arc (~0 to 125 km: east–west; ~125 to 475 km: north-northeast–south-southwest; ~475 km and above: west-northwest–east-southeast; distance is relative to MFT). The sharp transition of fast polarization directions from convergence-parallel to orogen-parallel directions at ~450 to 500 km north of the MFT marks the northern boundary of the Indian lower crust currently lying beneath Tibet, where basal shearing imposed by the lower plate ceases to have effect. Such a long travel distance at shallow depths suggests the Indian slab underthrusts rather than subducts under the plateau, hence suggesting that slab pull is not a potential driver for present-day continental collision in Tibet. In addition, this study confirms that basal shear force is the principal contributor to enabling southern Tibetan rifting and that present-day large-scale eastward flow is unlikely to be well developed beneath southern Tibet.

Data and Resources

The MATLAB (www.mathworks.com/products/matlab, last accessed July 2024) scripts used in the harmonic fitting of *Pms* moveout on receiver functions are available at doi: 10.5281/zenodo.7641812. The waveform data for *P*-wave receiver functions (P-RFs) obtained in this study can be available from the corresponding author upon reasonable request. The supplemental material for this article includes additional figures that provide further details for the crustal anisotropy measurements.

Declaration of Competing Interests

The authors acknowledge that there are no conflicts of interest recorded.

Acknowledgments

This study is supported by the National Natural Science Foundation of China under Grant Numbers 42374055 and U22B6002, 41774045, and the National Key Research and Development Program of China under Grant Number 2019YFA0708604. The authors thank Editor-in-Chief Allison Bent, Romain Jolivet, and two anonymous reviewers for their constructive suggestions and remarkable comments, which were helpful in improving this article.

References

Ader, T., J.-P. Avouac, J. Liu-Zeng, H. Lyon-Caen, L. Bollinger, J. Galetzka, J. Genrich, M. Thomas, K. Chanard, S. N. Sapkota, *et al.* (2012). Convergence rate across the Nepal Himalaya and interseismic coupling on the Main Himalayan Thrust: Implications for seismic hazard, *J. Geophys. Res.* **117,** no. B4, doi: 10.1029/2011JB009071.

Ammon, C. J. (1991). The isolation of receiver effects from teleseismic P waveforms, *Bull. Seismol. Soc. Am.* **81,** 2504–2510.

Bao, X., X. Song, D. W. Eaton, Y. Xu, and H. Chen (2020). Episodic lithospheric deformation in eastern Tibet inferred from seismic anisotropy, *Geophys. Res. Lett.* **47,** e2019GL085721, doi: 10.1029/2019GL085721.

Bao, X., X. Song, and J. Li (2015). High-resolution lithospheric structure beneath Mainland China from ambient noise and earthquake surface-wave tomography, *Earth Planet. Sci. Lett.* **417,** 132–141.

Becker, T. W., and C. Faccenna (2011). Mantle conveyor beneath the Tethyan collisional belt, *Earth Planet. Sci. Lett.* **310,** 453–461.

Bird, P. (1991). Lateral extrusion of lower crust from under high topography in the isostatic limit, *J. Geophys. Res.* **96,** 10,275–10,286.

Bischoff, S. H., and L. M. Flesch (2018). Normal faulting and viscous buckling in the Tibetan Plateau induced by a weak lower crust, *Nat. Commun.* **9,** 4952.

Chen, M., F. Niu, J. Tromp, A. Lenardic, C.-T. A. Lee, W. Cao, and J. Ribeiro (2017). Lithospheric foundering and underthrusting imaged beneath Tibet, *Nat. Commun.* **8,** 15,659.

Chen, W., and Y. Jiang (2020). Undulating Moho beneath a near-uniform surface of central Tibet, *Earth Planet. Sci. Lett.* **543,** 116,343.

Chen, W., M. Martin, T. Tseng, R. L. Nowack, S. Hung, and B. Huang (2010). Shear-wave birefringence and current configuration of converging lithosphere under Tibet, *Earth Planet. Sci. Lett.* **295,** 297–304.

Chen, Y., and F. Niu (2013). Ray-parameter based stacking and enhanced pre-conditioning for stable inversion of receiver function data, *Geophys. J. Int.* **194,** 1682–1700.

Cheng, S., X. Xiao, J. Wu, W. Wang, L. Sun, X. Wang, and L. Wen (2022). Crustal thickness and Vp/Vs variation beneath continental China revealed by receiver function analysis, *Geophys. J. Int.* **228,** 1731–1749.

Copley, A., J.-P. Avouac, and B. P. Wernicke (2011). Evidence for mechanical coupling and strong Indian lower crust beneath southern Tibet, *Nature* **472,** 79–81.

Dal Zilio, L., R. Jolivet, and Y. Dinthervan (2020). Segmentation of the Main Himalayan Thrust illuminated by Bayesian inference of interseismic coupling, *Geophys. Res. Lett.* **47,** e2019GL086424, doi: 10.1029/2019GL086424.

Ding, L., P. Kapp, F. Cai, C. N. Garzione, Z. Xiong, H. Wang, and C. Wang (2022). Timing and mechanisms of Tibetan Plateau uplift, *Nat. Rev. Earth Environ.* **3,** 652–667.

Fan, G., and T. Lay (2003). Strong Lg attenuation in the Tibetan Plateau, *Bull. Seismol. Soc. Am.* **93,** 2264–2272.

Gan, W., P. Zhang, Z. Shen, Z. Niu, M. Wang, Y. Wan, D. Zhou, and J. Cheng (2007). Present-day crustal motion within the Tibetan Plateau inferred from GPS measurements, *J. Geophys. Res.* **112,** no. B8, doi: 10.1029/2005JB004120.

Gao, R., Z. Lu, S. L. Klemperer, H. Wang, S. Dong, W. Li, and H. Li (2016). Crustal-scale duplexing beneath the Yarlung Zangbo suture in the western Himalaya, *Nature Geosci.* **9,** 555–560.

Gilligan, A., K. F. Priestley, S. W. Roecker, V. Levin, and S. S. Rai (2015). The crustal structure of the western Himalayas and Tibet, *J. Geophys. Res.* **120,** 3946–3964.

Gong, J., J. Li, and M. Li (2023). Isolated crustal partial melting in the southern Tibetan Plateau from H-κ-c method, *Geophys. Res. Lett.* **50,** e2023GL106363, doi: 10.1029/2023GL106363.

Guo, T., and Y. Gao (2020). Seismic anisotropy in the upper crust within Tibetan Plateau revealed by shear-wave splitting, *Chin. J. Geophys.* **63,** 1085–1103.

Guo, X., W. Li, R. Gao, X. Xu, H. Li, X. Huang, Z. Ye, Z. Lu, and S. L. Klemperer (2017). Nonuniform subduction of the Indian crust beneath the Himalayas, *Sci. Rep.* **7,** 12,497.

Hacker, B. R., E. Gnos, L. Ratschbacher, M. Grove, M. McWilliams, S. V. Sobolev, J. Wan, and Z. Wu (2000). Hot and dry deep crustal xenoliths from Tibet, *Science* **287,** 2463–2466.

Hajra, S., D. Hazarika, S. Mondal, S. K. Pal, and P. N. S. Roy (2022). Deformation of the upper crust in the Kumaon Himalaya analyzed from seismic anisotropy and gravity lineament studies, *Phys. Earth Planet. In.* **322,** 106,827.

Hayes, G. P., G. L. Moore, D. E. Portner, M. Hearne, H. Flamme, M. Furtney, and G. M. Smoczyk (2018). Slab2, a comprehensive subduction zone geometry model, *Science* **362,** 58–61.

Hetényi, G., R. Cattin, F. Brunet, L. Bollinger, J. Vergne, J. L. Nábělek, and M. Diament (2007). Density distribution of the India plate beneath the Tibetan plateau: Geophysical and petrological constraints on the kinetics of lower-crustal eclogitization, *Earth Planet. Sci. Lett.* **264,** 226–244.

Hu, X., E. Garzanti, J. Wang, W. Huang, W. An, and A. Webb (2016). The timing of India-Asia collision onset—Facts, theories, controversies, *Earth Sci. Rev.* **160,** 264–299.

Huang, C., L. Chang, and Z. Ding (2021). Crustal anisotropy in the eastern Himalayan syntaxis and adjacent areas, *Chin. J. Geophys.* **64,** 3970–3982.

Huang, S., H. Yao, Z. Lu, X. Tian, Y. Zheng, R. Wang, S. Luo, and J. Feng (2020). High-resolution 3-D shear wave velocity model of the Tibetan Plateau: Implications for crustal deformation and porphyry Cu deposit formation, *J. Geophys. Res.* **125,** e2019JB019215, doi: 10.1029/2019JB019215.

Huang, T. Y., Y. Gung, B. Y. Kuo, L. Y. Chiao, and Y. N. Chen (2015). Layered deformation in the Taiwan orogen, *Science* **349,** 720–723.

Jiang, G., S. Hu, Y. Shi, C. Zhang, Z. Wang, and D. Hu (2019). Terrestrial heat flow of continental China: Updated dataset and tectonic implications. *Tectonophysics* **753,** 36–48.

Jiao, L., P. Tapponnier, A. Mccallum Coudurier-Curveur, and X. Xu (2024). The shape of the Himalayan "Arc": An ellipse pinned by syntaxial strike-slip fault tips, *Proc. Natl. Acad. Sci. Unit. States Am.* **121,** e2313278121, doi: 10.1073/pnas.2313278121.

Jin, S., Y. Sheng, M. J. Comeau, M. Becken, W. Wei, G. Ye, H. Dong, and L. Zhang (2022). Relationship of the crustal structure, rheology, and tectonic dynamics beneath the Lhasa-Gangdese terrane (southern Tibet) based on a 3-D electrical model, *J. Geophys. Res.* **127,** e2022JB024318, doi: 10.1029/2022JB024318.

Kanaujia, J., S. Mitra, S. C. Gupta, and M. L. Sharma (2019). Crustal anisotropy from shear-wave splitting of local earthquakes in the Garhwal Lesser Himalaya, *Geophys. J. Int.* **219,** 2013–2033.

Kind, R., X. Yuan, J. Saul, D. Nelson, S. V. Sobolev, J. Mechie, W. Zhao, G. Kosarev, J. Ni, U. Achauer, *et al.* (2002). Seismic images of crust and upper mantle beneath Tibet: Evidence for Eurasian plate subduction, *Science* **298,** 1219–1221.

Klemperer, S. L., P. Zhao, C. J. Whyte, T. H. Darrah, L. J. Crossey, K. E. Karlstrom, T. Liu, C. Winn, D. R. Hilton, *et al.* (2022). Limited underthrusting of India below Tibet: (3)He/(4)He analysis of thermal springs locates the mantle suture in continental collision, *Proc. Natl. Acad. Sci. Unit. States Am.* **119,** e2113877119, doi: 10.1073/pnas.2113877119.

Ko, B., and H. Jung (2015). Crystal preferred orientation of an amphibole experimentally deformed by simple shear, *Nat. Commun.* **6,** 6586.

Li, C., R. D. van der Hilst, A. S. Meltzer, and E. R. Engdahl (2008). Subduction of the Indian lithosphere beneath the Tibetan Plateau and Burma, *Earth Planet. Sci. Lett.* **274,** 157–168.

Li, J., and X. Song (2018). Tearing of Indian mantle lithosphere from high-resolution seismic images and its implications for lithosphere coupling in southern Tibet, *Proc. Natl. Acad. Sci. Unit. States Am.* **115,** 8296–8300.

Li, J., X. Song, P. Wang, and L. Zhu (2019). A generalized H-κ method with harmonic corrections on Ps and its crustal multiples in receiver functions, *J. Geophys. Res.* **124,** 3782–3801.

Li, S., T. Tao, F. Gao, X. Qu, Y. Zhu, and J. Huang (2022). Present-day fault kinematic around the eastern Himalayan Syntaxis and probable viscoelastic relaxation perturbation following the 1950 Mw 8.7 Assam earthquake, *J. Asian Earth Sci.* **238,** 105,396.

Li, Z. (2013). A review on the numerical geodynamic modeling of continental subduction, collision and exhumation, *Sci. China Earth Sci.* **57,** 47–69.

Li, Z., F. Cui, S. Yang, and X. Zhong (2023). Key geodynamic processes and driving forces of Tethyan evolution, *Sci. China Earth Sci.* **66,** 2666–2685.

Liang, X., L. Chen, X. Tian, Y. Chu, and W. Li (2023). Uplifting mechanism of the Tibetan Plateau inferred from the characteristics of crustal structures, *Sci. China Earth Sci.* **66,** 2770–2790.

Liu, H., and F. Niu (2012). Estimating crustal seismic anisotropy with a joint analysis of radial and transverse receiver function data, *Geophys. J. Int.* **188,** 144–164.

Liu, S., J. Yang, and Y. Zheng (2023). Study on shear wave splitting of local earthquakes in Namche Barwa, *Chin. J. Geophys.* **66,** 3692–3703.

Liu, Z., J. Park, and D. M. Rye (2015). Crustal anisotropy in northeastern Tibetan Plateau inferred from receiver functions: Rock textures caused by metamorphic fluids and lower crust flow? *Tectonophysics* **661,** 66–80.

Long, M. D., and P. G. Silver (2008). The subduction zone flow field from seismic anisotropy: A global view, *Science* **319,** 315–318.

Lü, Y., S. Ni, B. Liu, and Y. Sun (2011). Pn tomographic velocity and anisotropy beneath the Tibetan Plateau and the adjacent regions, *Earth Planets Space* **63,** 1169–1173.

Luo, Y., M. D. Long, F. Link, P. Karabinos, and Y. D. Kuiper (2023). Insights from layered anisotropy beneath southern New England: From ancient tectonism to present-day mantle flow, *Geochem. Geophys. Geosys.* **24,** e2023GC011118, doi: 10.1029/2023GC011118.

Mahan, K. (2006). Retrograde mica in deep crustal granulites: Implications for crustal seismic anisotropy, *Geophys. Res. Lett.* **33,** L24301, doi: 10.1029/2006GL028130.

McKenzie, D., and J. Jackson (2002). Conditions for flow in the continental crust, *Tectonics* **21,** 5-1–5-7.

Meissner, R., W. D. Mooney, and I. Artemieva (2002). Seismic anisotropy and mantle creep in young orogens, *Geophys. J. Int.* **149,** 1–14.

Nábělek, J., G. Hetényi, J. Vergne, S. Sapkota, B. Kafle, M. Jiang, H. Su, J. Chen, B.-S. Huang, and , and The Hi-Climb Team (2009). Underplating in the Himalaya-Tibet collision zone revealed by the Hi-CLIMB experiment, *Science* **325,** 1371–1374.

Nagaya, M., H. Oda, H. Akazawa, and M. Ishise (2008). Receiver functions of seismic waves in layered anisotropic media: Application to the estimate of seismic anisotropy, *Bull. Seismol. Soc. Am.* **98,** 2990–3006.

Nie, S., J. Li, C. Wu, and P. Tan (2023). Formation of the V-shaped conjugate strike-slip faults revealed by crustal anisotropy in the central Tibetan Plateau, *J. Asian Earth Sci.* **258,** 105725.

Nie, S., X. Tian, X. Liang, and B. Wan (2023). Less-well-developed crustal channel-flow in the central Tibetan Plateau revealed by receiver function and surface wave joint inversion, *J. Geophys. Res.* **128,** e2022JB025747, doi: 10.1029/2022JB025747.

Ozacar, A. A., and G. Zandt (2004). Crustal seismic anisotropy in central Tibet: Implications for deformational style and flow in the crust, *Geophys. Res. Lett.* **31,** L23601, doi: 10.1029/2004GL021096.

Pandey, S., X. Yuan, E. Debayle, F. Tilmann, K. Priestley, and X. Li (2015). Depth-variant azimuthal anisotropy in Tibet revealed by surface wave tomography, *Geophys. Res. Lett.* **42,** 4326–4334.

Paul, A., D. Hazarika, and M. Wadhawan (2017). Shear wave splitting and crustal anisotropy in the Eastern Ladakh-Karakoram zone, northwest Himalaya, *J. Asian Earth Sci.* **140,** 122–134.

Reiss, M. C., G. Rümpker, and I. Wölbern (2018). Large-scale trench-normal mantle flow beneath central South America, *Earth Planet. Sci. Lett.* **482,** 115–125.

Roy, S. K., D. Srinagesh, G. Suresh, and D. Srinivas (2021). Disparate deformation of the crust and upper mantle beneath the Doda-Kisthwar region, NW Himalaya, *Phys. Earth Planet. In.* **310,** 106,635.

Rümpker, G., A. Kaviani, and K. Latifi (2014). Ps-splitting analysis for multilayered anisotropic media by azimuthal stacking and layer stripping, *Geophys. J. Int.* **199,** 146–163.

Russo, R. M., and P. G. Silver (1994). Trench-parallel flow beneath the Nazca plate from seismic anisotropy, *Science* **263,** 1105–1111.

Saikia, S., M. Wadhawan, A. Sharma, and S. Baruah (2022). Analysis of crustal seismic anisotropy of the Eastern Himalayan collision zone and its adjoining regions, *J. Asian Earth Sci.* **226,** 105,085.

Savage, M. K. (1999). Seismic anisotropy and mantle deformation: What have we learned from shear wave splitting? *Rev. Geophys.* **37,** 65–106.

Schulte-Pelkum, V., G. Monsalve, A. Sheehan, M. R. Pandey, S. Sapkota, R. Bilham, and F. Wu (2005). Imaging the Indian subcontinent beneath the Himalaya, *Nature* **435,** 1222–1225.

Sherrington, H. F., G. Zandt, and A. Frederiksen (2004). Crustal fabric in the Tibetan Plateau based on waveform inversions for seismic anisotropy parameters, *J. Geophys. Res.* **109,** no. B2, doi: 10.1029/2002JB002345.

Shi, D., S. L. Klemperer, J. Shi, Z. Wu, and W. Zhao (2020). Localized foundering of Indian lower crust in the India-Tibet collision zone, *Proc. Natl. Acad. Sci. Unit. States Am.* **117,** 24,742–24,747.

Shi, D., W. Zhao, S. L. Klemperer, Z. Wu, J. Mechie, J. Shi, G. Xue, and H. Su (2016). West–east transition from underplating to steep subduction in the India–Tibet collision zone revealed by receiver-function profiles, *Earth Planet. Sci. Lett.* **452,** 171–177.

Silver, P. G. (1996). Seismic anisotropy beneath the continents: Probing the depths of geology, *Annu. Rev. Earth Planet. Sci.* **24,** 385–432.

Tan, P., X. Liang, W. Li, and C. Wu (2023). Crustal structure of the Tibetan Plateau and adjacent areas revealed from ambient noise tomography, *Gondwana Res.* **121,** 1–15.

Tapponnier, P., Z. Xu, F. Roger, B. Meyer, N. Arnaud, G. Wittlinger, and J. Yang (2001). Oblique stepwise rise and growth of the Tibet Plateau, *Science* **294,** 1671–1677.

Tatham, D. J., G. E. Lloyd, R. W. H. Butler, and M. Casey (2008). Amphibole and lower crustal seismic properties, *Earth Planet. Sci. Lett.* **267,** 118–128.

Taylor, M., and A. Yin (2009). Active structures of the Himalayan-Tibetan orogen and their relationships to earthquake distribution, contemporary strain field, and Cenozoic volcanism, *Geosphere* **5,** 199–214.

van Hinsbergen, D. J. J., P. C. Lippert, S. Li, W. Huang, E. L. Advokaat, and W. Spakman (2019). Reconstructing Greater India: Paleogeographic, kinematic, and geodynamic perspectives, *Tectonophysics* **760,** 69–94.

Wadhawan, M., D. Hazarika, A. Paul, N. Kumar, V. Gupta, and M. Agarwal (2022). Seismic anisotropy and crustal deformation in the Satluj valley and adjoining region of northwest Himalaya revealed by the splitting analysis of Moho converted Ps phases, *J. Asian Earth Sci.* **238,** 105,377.

Wang, G., H. Thybo, and I. M. Artemieva (2021). No mafic layer in 80 km thick Tibetan crust, *Nat. Commun.* **12,** 1069.

Wang, K., L. Chang, and Z. Ding (2021). Upper crustal anisotropy in the eastern Himalayan syntaxis, *Acta Seismol. Sin.* **43,** 168–179.

Wei, W., M. Unsworth, A. Jones, J. Booker, H. Tan, D. Nelson, L. Chen, S. Li, K. Solon, P. Bedrosian, *et al.* (2001). Detection of widespread fluids in the Tibetan crust by magnetotelluric studies, *Science* **292,** 716–719.

Wu, C., X. Tian, T. Xu, X. Liang, Y. Chen, M. Taylor, J. Badal, Z. Bai, Y. Duan, G. Yu, *et al.* (2019). Deformation of crust and upper mantle in central Tibet caused by the northward subduction and slab tearing of the Indian lithosphere: New evidence based on shear wave splitting measurements, *Earth Planet. Sci. Lett.* **514,** 75–83.

Wu, C., X. Tian, T. Xu, X. Liang, Y. Chen, G. Zhu, J. Badal, Z. Bai, G. Yu, and J. Teng (2019). Upper-crustal anisotropy of the conjugate strike-slip fault zone in central Tibet analyzed using local earthquakes and shear-wave splitting, *Bull. Seismol. Soc. Am.* **109,** 1968–1984.

Wu, F., B. Wan, L. Zhao, W. Xiao, and R. Zhu (2020). Tethyan geodynamics, *Acta Petrol. Sin.* **36,** 1627–1674.

Wu, J., Z. Zhang, F. Kong, B. B. Yang, Y. Yu, K. H. Liu, and S. S. Gao (2015). Complex seismic anisotropy beneath western Tibet and its geodynamic implications, *Earth Planet. Sci. Lett.* **413,** 167–175.

Wu, Y., X. Bao, B. Zhang, Y. Xu, and W. Yang (2022). Seismic evidence for stepwise lithospheric delamination beneath the Tibetan Plateau, *Geophys. Res. Lett.* **49,** e2022GL098528, doi: 10.1029/2022GL098528.

Xie, C., S. Jin, W. Wei, G. Ye, L. Zhang, H. Dong, and Y. Yin (2017). Varying Indian crustal front in the southern Tibetan Plateau as revealed by magnetotelluric data, *Earth Planets Space* **69,** 147.

Xu, Q., L. Ding, S. Pei, X. Yuan, J. Zhao, H. Liu, H. Liu, L. Li, and H. Zuo (2022). Underthrusting and pure shear mechanisms dominate the crustal deformation beneath the core of the Eastern Himalayan Syntaxis as inferred from high-resolution receiver function imaging, *Geophys. Res. Lett.* **49,** e2022GL101697, doi: 10.1029/2022GL101697.

Xu, Q., J. Zhao, X. Yuan, H. Liu, and S. Pei (2017). Detailed configuration of the underthrusting Indian lithosphere beneath western Tibet revealed by receiver function images, *J. Geophys. Res.* **122,** 8257–8269.

Xuan, S., and S. Jin (2022). Moho depth and crustal density structure in the Tibetan Plateau from gravity data modelling, *J. Asian Earth Sci.* **233,** 105261.

Yang, G., L. Chen, L. Zhao, X. Xie, and Z. Yao (2023). Crustal Lg attenuation beneath the Iranian Plateau: Implications for Cenozoic magmatism related to slab subduction, slab break-off, and mantle flow, *J. Geophys. Res.* **128,** e2022JB025664, doi: 10.1029/2022JB025664.

Yang, Y., M. H. Ritzwoller, Y. Zheng, W. Shen, A. L. Levshin, and Z. Xie (2012). A synoptic view of the distribution and connectivity of the mid-crustal low velocity zone beneath Tibet, *J. Geophys. Res.* **117,** no. B4, doi: 10.1029/2011JB008810.

Yin, A. (2000). Mode of Cenozoic east-west extension in Tibet suggesting a common origin of rifts in Asia during the Indo-Asian collision, *J. Geophys. Res.* **105,** 21,745–21,759.

Zhang, B., X. Bao, Y. Wu, Y. Xu, and W. Yang (2023). Southern Tibetan rifting since late Miocene enabled by basal shear of the underthrusting Indian lithosphere, *Nat. Commun.* **14,** 2565.

Zhang, B., X. Bao, and Y. Xu (2022). Seismic anisotropy in Central Tien Shan unveils rheology-controlled deformation during intracontinental orogenesis, *Geology* **50,** 812–816.

Zhang, Z., and X. Tian (2011). Anisotropy of the crust and upper mantle beneath the central Tibetan plateau, *Chin. J. Geophys.* **54,** 2761–2768.

Zhang, Z., L. Ding, Z. Zhao, and M. Santosh (2017). Tectonic evolution and dynamics of the Tibetan Plateau, *Gondwana Res.* **41,** 1–8.

Zhang, Z., Y. Wang, G. A. Houseman, T. Xu, Z. Wu, X. Yuan, Y. Chen, X. Tian, Z. Bai, and J. Teng (2014). The Moho beneath western Tibet: Shear zones and eclogitization in the lower crust, *Earth Planet. Sci. Lett.* **408,** 370–377.

Zhao, G., J. Liu, B. Chen, M. K. Kaban, and X. Zheng (2020). Moho beneath Tibet based on a joint analysis of gravity and seismic data, *Geochem. Geophys. Geosys.* **21,** e2019GC008849, doi: 10.1029/2019GC008849.

Zhao, L., A. Paul, S. Guillot, S. Solarino, M. G. Malusà, T. Zheng, C. Aubert, S. Salimbeni, T. Dumont, S. Schwartz, *et al.* (2015). First seismic evidence for continental subduction beneath the Western Alps, *Geology* **43,** 815–818.

Zhao, L., X. Xie, J. He, X. Tian, and Z. Yao (2013). Crustal flow pattern beneath the Tibetan Plateau constrained by regional Lg-wave Q tomography, *Earth Planet. Sci. Lett.* **383,** 113–122.

Zheng, Y. (2012). Metamorphic chemical geodynamics in continental subduction zones, *Chem. Geol.* **328,** 5–48.

Manuscript received 15 March 2024
Published online 2 August 2024